remote sensing

MDPI

Article

Detection and Quantification of Irrigation Water Amounts at 500 m Using Sentinel-1 Surface Soil Moisture

Luca Zappa [1,*], Stefan Schlaffer [1], Bernhard Bauer-Marschallinger [1], Claas Nendel [2], Beate Zimmerman [3] and Wouter Dorigo [1]

[1] Department of Geodesy and Geoinformation, TU Wien, Wiedner Hauptstrasse 8, 1040 Vienna, Austria; stefan.schlaffer@geo.tuwien.ac.at (S.S.); Bernhard.Bauer-Marschallinger@geo.tuwien.ac.at (B.B.-M.); wouter.dorigo@geo.tuwien.ac.at (W.D.)

[2] Research Platform Data Analysis and Simulation, Leibniz Centre for Agricultural Landscape Research (ZALF), Eberswalderstrasse 84, 15374 Muencheberg, Germany; nendel@zalf.de

[3] Forschungsinstitut für Bergbaufolgelandschaften e.V., Brauhausweg 2, 03238 Finsterwalde, Germany; b.zimmermann@fib-ev.de

* Correspondence: luca.zappa@geo.tuwien.ac.at; Tel.: +43-1-58801-12289

Abstract: Detailed information about irrigation timing and water use at a high spatial resolution is critical for monitoring and improving agricultural water use efficiency. However, neither statistical surveys nor remote sensing-based approaches can currently accommodate this need. To address this gap, we propose a novel approach based on the TU Wien Sentinel-1 Surface Soil Moisture product, characterized by a spatial sampling of 500 m and a revisit time of 1.5–4 days over Europe. Spatiotemporal patterns of soil moisture are used to identify individual irrigation events and estimate irrigation water amounts. To retrieve the latter, we include formulations of evapotranspiration and drainage losses to account for vertical fluxes, which may significantly influence sub-daily soil moisture variations. The proposed approach was evaluated against field-scale irrigation data reported by farmers at three sites in Germany with heterogeneous field sizes, crop patterns, irrigation systems and management. Our results show that most field-scale irrigation events can be detected using soil moisture information (mean F-score = 0.77). Irrigation estimates, in terms of temporal dynamics as well as spatial patterns, were in agreement with reference data (mean Pearson correlation = 0.64) regardless of field-specific characteristics (e.g., crop type). Hence, the proposed approach has the potential to be applied over large regions with varying cropping systems.

Keywords: irrigation; Sentinel-1; surface soil moisture; high resolution; remote sensing; Northern Germany

Citation: Zappa, L.; Schlaffer, S.; Bauer-Marschallinger, B.; Nendel, C.; Zimmerman, B.; Dorigo, W. Detection and Quantification of Irrigation Water Amounts at 500 m Using Sentinel-1 Surface Soil Moisture. *Remote Sens.* **2021**, *13*, 1727. https://doi.org/10.3390/rs13091727

Academic Editor: Giorgio Baiamonte

Received: 2 March 2021
Accepted: 27 April 2021
Published: 29 April 2021

1. Introduction

Irrigated agriculture plays a key role in ensuring food security by providing approximately 40% of the world's food, despite covering only 20% of cropland globally [1,2]. For instance, global cereal production would decrease by 20% without irrigation [3]. Irrigated agriculture is responsible for more than 70% of freshwater withdrawals worldwide [4,5], which in many cases leads to, e.g., groundwater depletion [6,7], soil salinization [8], degradation of freshwater bodies [9] and nitrous oxide emissions [10]. By influencing the surface water and energy balances by increasing soil moisture, irrigation is also an important climate forcing [11,12]. The increased evapotranspiration (ET) driven by irrigation has a regional cooling effect on land surface temperature [11,13], thus potentially masking the full global warming signal on local and regional scales [14]. Global warming and the expected change of precipitation patterns [15] resulting in a decrease of water availability especially in already water-scarce regions will intensify the need for irrigation [16–18]. This complex scenario will be further exacerbated by the increased needs of a more populous world with rising living standards [19].

Despite the importance of irrigation in the water–energy–food nexus, detailed information on water volumes used in irrigated agriculture is still missing. Statistical surveys are highly uncertain due to self-reporting bias, low temporal resolution and spatial inconsistencies [20]. When available, irrigation statistics are usually delivered with a delay of 1–3 years, spatially aggregated to regional or national scale and their quality is highly variable [21]. Furthermore, such surveys do not account for illegal water abstractions [22].

Satellite remote sensing is emerging as a convenient means to map and quantify irrigation water volumes, overcoming many of the mentioned limitations [23]. Optical and thermal remote sensing have been used to estimate actual evapotranspiration (ET), which can be coupled to the water-energy balance allowing to estimate irrigation volumes [24–29]. However, such observations are strongly affected by cloud conditions and atmospheric transmissivity, limiting their use over regions characterized by frequent cloud cover [30]. Being a natural source of information on the amount of water entering the ground, soil moisture is directly related to irrigation and precipitation. Ground measurements of soil moisture have demonstrated great potential to accurately track and quantify irrigation [31]. Soil moisture derived from spaceborne microwave sensors has been used for the same purpose [32–36]. However, the coarse spatial resolution of most soil moisture products represents a major constraint for accurate irrigation water use retrieval [32,35]. In fact, the irrigation signal of individual fields (most European fields range between 0.1 and 2 km^2) cannot be detected by current coarse resolution products (pixel size in the order of 20 km $\times$ 20 km) as it is mixed with several other features, such as non-irrigated fields, various land cover and land use types, mountains and valleys and water bodies [37].

The Sentinel-1 mission currently provides the richest freely available Synthetic Aperture Radar (SAR) data source in terms of spatial resolution and revisit time [38,39]. The payload of Sentinel-1 consists of a C-band sensor that is sensitive to changes in surface soil moisture. Therefore, the retrieved Surface Soil Moisture product (S1-SSM) at 500 m sampling through the TU Wien change detection method [40] has the potential to allow monitoring irrigation on a (quasi) field scale. However, the temporal resolution of 1.5–4 days (over Europe) represents a challenge compared to coarse scale products, as the irrigation signal might no longer be visible after such a long interval [31,41]. Furthermore, methods to estimate irrigation water volumes developed for coarse scale products are not well suited for high-resolution datasets. For instance, Zaussinger et al. (2019) developed a framework exploiting the difference between remotely sensed and modeled soil moisture, based on the assumption that the model does not include the irrigation signal, while satellite observations do. Applying such an approach with S1-SSM would require a modeled soil moisture dataset with comparable spatial resolution, i.e., based on accurate forcing data at the kilometric scale. Alternatively, the SM2RAIN algorithm [42] has been used to retrieve irrigation by subtracting rainfall from the total amount of water estimated to enter the soil [32,33]. In addition, in this case, rainfall data at a comparable spatial resolution (<1 km) would be necessary to derive irrigation water amounts. Unfortunately, neither modeled soil moisture nor rainfall observations exist at the (sub-)kilometric scale over Europe, let alone globally. Even though catchment- and region-specific datasets are available, such localized datasets differ in terms of, e.g., representation of the water balance, parameterization, modeled variables (e.g., depth) and measurement technique, making regional results not comparable [43–45].

Hence, currently available information on irrigation, i.e., from statistical surveys, optical, thermal and microwave remote sensing, is of limited value for a spatially detailed assessment or a timely monitoring of agricultural water use. In this paper, we propose a novel approach exploiting the spatiotemporal patterns of the Vienna University of Technology (TU Wien) S1-SSM product in order to fill this gap, i.e., to detect individual irrigation events and to quantify irrigation water amounts at a resolution of 500 m. Ideally, such information should be derivable and consistent for any region, hence no additional datasets (e.g., meteorological stations, modeled soil moisture and rainfall observations) should be required. Hence, soil moisture dynamics of individual pixels were compared against the

surrounding area, as irrigation occurring in a specific field (pixel) should be reflected by a local increase in soil moisture, while the surrounding rainfed fields (pixels) exhibit a different behavior. Our approach was tested and evaluated against field scale irrigation water amounts reported by farmers at three sites in northeastern Germany, characterized by different field sizes, cultivated crops and irrigation systems.

2. Materials

2.1. Study Sites

The analysis and assessment of the proposed method were carried out over three sites located in Germany, hereafter referred to as Brandenburg_1 (BB1), Brandenburg_2 (BB2) and Niedersachsen (NS) (Figure 1). According to the Koeppen–Geiger classification [46], all sites have a Temperate Oceanic Climate (Cfb class). Temperature and precipitation measurements for each site were acquired from the closest meteorological station through the German Weather Service (DWD) Climate Data Center (CDC). Mean annual temperature and precipitation for the study sites are approximately 9 °C and 550 mm, respectively. The area is characterized by slightly higher precipitation during summer months compared to the rest of the year. Similar soil conditions are found over the three test sites, with sand content of approximately 55%, followed by silt (30%) and clay (15%) [47]. Hence, the predominant soil texture class of the study sites is sandy loam [48]. The diversity of cropping patterns in the investigated fields is reflected in the irrigation management, which varies greatly in terms of frequency, amount of water distributed and the overall irrigation period. Detailed information about the individual sites, directly provided by farmers, is given below.

The BB1 site is composed of four center pivot fields ranging between 34 and 50 ha. Reported irrigation doses for these fields are in the order of 15 mm per event; however, exact measurements were not available. Dates of individual irrigation events were provided for the 2018 growing season, recording a total of 48 irrigation events (i.e., on average 12 events per field). The following crops were cultivated: potato, winter wheat and pea.

Eighteen center pivot fields constitute the BB2 site. The field size is on average 37.7 ha, and ranges between 12 and 116 ha. Dates of irrigation and related water amounts (expressed in mm) throughout the 2019 growing season were reported for each field. The average number of irrigation events per field was 6.4, with 27 mm of water distributed per event. Grain maize was cultivated on half of the fields, while cereals (wheat, oat and rye) and sugar beet were grown on the remaining fields.

The NS site comprises 49 fields, ranging from <1.5 to >30 ha (mean field size of 8.3 ha). Irrigation dates and volumes for 2018, provided for each field were converted into water heights. In total, 1168 irrigation events were reported for the NS site, with an average of 23.8 events per field and 13 mm of water per event. The dominant crops cultivated were potato, sugar beet, summer barley and winter wheat. The irrigation system is not known.

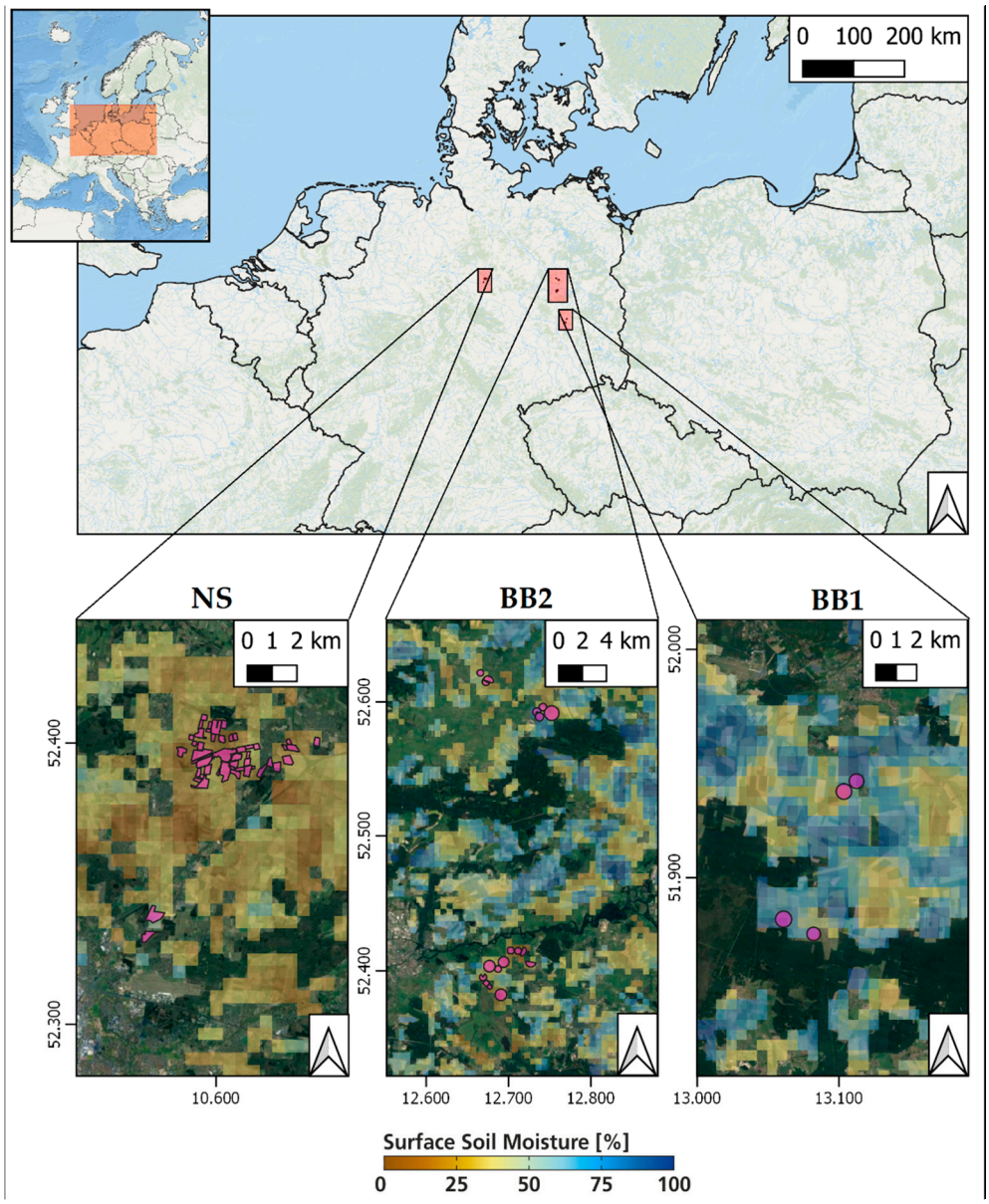

Figure 1. Location of the three study sites (base map from ESRI) and zoomed-in view of the individual sites and fields (base map from Google). Sentinel-1 Surface Soil Moisture maps for 7 June 2018, with non-agricultural pixels masked, are also shown.

2.2. Sentinel-1 Surface Soil Moisture

The Sentinel-1 mission consists of two identical satellites, Sentinel-1A and Sentinel-1B, launched in 2014 and 2016, respectively. The C-band SAR sensor onboard the satellites provides in the Interferometric Wide swath mode backscatter observations with a Ground Range Detected (GRD) nominal resolution of 20 m and 1 dB radiometric accuracy [40]. The mission observation scenario assures that each land location on the globe is observed within 12 days. With both satellites in orbit, the European land and coastal waters are systematically mapped within the constellation's 6-day repeat cycle, in both ascending and descending passes. However, with increasing latitude, a particular location might be covered by two or more acquisition geometries, and the temporal resolution improves over Europe to 1.5–4 days [40].

In this study, we used the 500 m-sampled Surface Soil Moisture product from Sentinel-1 (S1-SSM) retrieved with the TU Wien change detection method [40], which serves as input to the Copernicus Global Land Service (CGLS) 1 km Surface Soil Moisture product (named

SSM1km). The latter is freely available and provided in Near-Real-Time (NRT) as daily composites for Europe at a 1 km sampling. The pre-processing and retrieval algorithm were described in detail by Bauer-Marschallinger et al. (2019) [40]. In short, the complexity of the field-scale backscatter signal dictates a spatial upscaling of backscatter to 500 m, at which scale the numerous features affecting the radar signal can be modeled robustly. The upscaled backscatter is normalized to a reference radar incidence angle, and then linearly scaled between localized dry and wet references. Hence, soil moisture is expressed in relative terms as degree of saturation, but it can be converted to volumetric soil moisture if information on soil porosity is available. Currently, the retrieved soil moisture product is not corrected for the influence of vegetation changes on the radar backscatter signal [40], potentially leading to seasonal vegetation biases.

In total, 227 S1-SSM pixels cover the three study sites; however, each satellite pixel covers a diverse portion of the irrigated fields (Figure 2), i.e., the fractional irrigated area. The latter is defined as the ratio between the area of irrigated field(s) observed by a S1-SSM pixel and the pixel area. The majority of S1-SSM pixels covers only a small portion, i.e., smaller than 20%, of the irrigated fields over all sites.

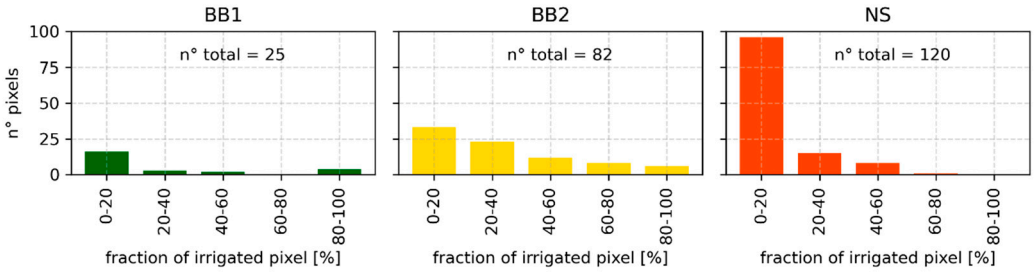

Figure 2. Number of S1-SSM pixels covering the reference irrigated fields, grouped by the pixel fractional irrigated area, i.e., the ratio between the irrigated area covered by a S1-SSM pixel and the pixel area.

2.3. Ancillary Datasets

The following ancillary datasets were resampled to 500 m and reprojected to the Equi7Grid projection [49].

The Corine Land Cover (CLC) maps, with a spatial resolution of 100 m, represent a complete and temporally consistent cartographic source of land use/land cover for Europe. Here, we employed the 5th CLC inventory (CLC2018), which depicts land cover for the period 2017–2018 [50]. To estimate irrigation water amounts, we considered only S1-SSM pixels potentially subject to irrigation. Hence, we masked all pixels covered less than 50% by the following CLC classes: non-irrigated arable land (Class 211) and permanently irrigated arable land (Class 212).

To monitor the vegetation status and development at each study site, we employed the Normalized Difference Vegetation Index (NDVI) obtained through the CGLS. The CGLS NDVI product is based on data acquired by PROBA-V and is provided at 1 km sampling as 10-day maximum value composite (https://land.copernicus.eu/global/products/ndvi, accessed on 24 February 2021). We applied a rolling mean with a window size of 35 days for noise reduction.

Information on soil porosity was used to convert the saturation degree provided by the S1-SSM product to volumetric units similarly to Al-Yaari et al. (2019) [51]. We obtained clay, sand and soil organic carbon content at 250 m resolution from the SoilGrids dataset [47] at 0 and 5 cm depth. After spatial resampling, these variables were used to compute soil porosity following the approach proposed by Saxton and Rawls (2006), who developed numerous empirical relationships based on extensive laboratory data [52].

3. Methods

3.1. Detection of Irrigation Events

3.1.1. Determining the Irrigation Period

The irrigation period can vary considerably between different sites and among individual fields, depending on the specific combination of crop type, phenology and meteorological conditions. Hence, we investigated how the definition of the period of the year potentially subject to irrigation, i.e., the irrigation period (IP), affects the detection of irrigation. The first method uses default dates ($IP_{default}$) for the start and end of season (SoS and EoS, respectively): here, we selected the period from 1 May to 1 September based on the most common timing of planting and harvesting for the major cultivars in the area [53]. The second solution analyzes the CGLS NDVI time series on a per-pixel basis to find most likely irrigation period based on the crop phenological development (IP_{NDVI}). For this method, we first identified the date of vegetative peak, i.e., maximum NDVI between May and August. Then, we determined the minimum NDVI values within four months before and after the peak. Following Atzberger et al. (2013) [54], we defined the start of season as the date with an NDVI value of at least 20% of the difference between the first minimum and the peak. The end of season was derived using the same criterion. Pixels characterized by an absolute difference in NDVI between the peak and the start of season smaller than 0.2 were disregarded, as well as pixels with a growing period (EoS–SoS) shorter than 75 days. The third method considers the ideal scenario in which the irrigation period for each pixel is known, i.e., obtained from the reported irrigation dates (IP_{actual}).

3.1.2. Identifying Irrigation Events

Then, we examined the temporal and spatial dynamics of soil moisture (SM) to pinpoint individual irrigation events occurring within the defined irrigation periods. If soil moisture increased between two consecutive acquisitions (at times $t-1$ and t), the latest observation was flagged as potential irrigation event. To discern irrigation from other factors causing a rise in soil moisture, e.g., precipitation and retrieval noise, we compared the relative soil moisture increase of a pixel to that of its surroundings. Such a criterion was preferred to other alternatives such as the comparison with rainfall as the spatial mismatch between the S1-SSM resolution (500 m) and the coarse scale of most rainfall datasets [55] would introduce an additional source of uncertainty. We calculated the relative soil moisture increase as:

$$\Delta SM_t = \frac{SM_t - SM_{t-1}}{SM_{t-1}} \quad (1)$$

both locally, i.e., to pixel i ($\Delta SM_{t,local}$), and for the surrounding agricultural area ($\Delta SM_{t,areal}$), defined as the $n \times n$ pixel grid around pixel i. We assessed the benefit of using larger spatial windows (n between 5 and 39 pixels, i.e., grid size between 2.5 and 19.5 km) compared to the smallest possible surrounding window (n = 3 pixels, i.e., grid size = 1.5 km) that served as benchmark. We assumed that meteorological conditions, e.g., precipitation and temperature, found in the surrounding area were identical to those found at pixel i. To ensure that potential differences between local and areal ΔSM estimates were not caused by differences in vegetation water content and structure, we considered only surrounding cells with NDVI values similar to pixel i. Hence, surrounding pixels were masked if the absolute NDVI difference was larger than 0.15, similarly to El-Hajj et al. (2017) [56]. $\Delta SM_{t,areal}$ was then computed as the mean of relative increases (ΔSM) of the unmasked surrounding pixels after discarding the lowest and highest 10% values. The truncation ensured that extreme ΔSM values, driven by, e.g., irrigation in surrounding fields and suspicious soil moisture retrievals, did not influence the mean.

Finally, the ratio between local and areal ΔSM was calculated. Values larger than 1 indicate that pixel i becomes wetter than the surrounding area, while a ratio smaller than 1 implies that, on average, soil moisture increases more in the adjacent pixels. Ideally, if an irrigation event occurs at pixel i, it would lead to a larger soil moisture increase compared to

the neighboring cells. Several thresholds, i.e., SM_{ratio_t}, for the identification of an irrigation event were tested, ranging from very inclusive (1.005) to conservative (1.6) values.

3.2. Quantification of Irrigation Water Amounts

For each detected event, the irrigation water amount was calculated as the soil moisture difference between the two consecutive satellite acquisitions (Equation (2)):

$$\text{Irrigation} = SM^{*}_{t,local} - SM_{t-1,local} \quad (2)$$

where $SM^{*}_{t,local}$ is the local soil moisture that would be found net of any precipitation contribution occurring during the same temporal window. In fact, both precipitation and irrigation can occur within the time between two consecutive Sentinel-1 acquisitions. Assuming that a rainfall event would lead to a soil moisture increase of the surrounding pixels (i.e., $\Delta SM_{t,areal} > 0$), we calculated:

$$\Delta SM^{*}_{t,local} = \begin{cases} \Delta SM_{t,local} - \Delta SM_{t,areal}\ , & | \ \Delta SM_{t,areal} > 0 \\ \Delta SM_{t,local}\ , & | \ \Delta SM_{t,areal} \leq 0 \end{cases} \quad (3)$$

$$SM^{*}_{t,local} = (SM_{t-1,local} \cdot \Delta SM^{*}_{t,local}) + SM_{t-1,local} \quad (4)$$

where $SM_{t-1,local}$ is the soil moisture found locally, i.e., at pixel i, before the irrigation event. Irrigation water volume was then converted to the corresponding water column depth (i.e., expressed in mm) by multiplying it with the depth of soil for which S1-SSM is representative [35], i.e., top 5 cm.

3.2.1. Accounting for Evapotranspiration

As sub-daily soil moisture variations cannot be captured due to the relatively low temporal resolution of Sentinel-1, irrigation would be largely underestimated. Therefore, we included simple formulations of evapotranspiration and drainage to adjust the retrieved irrigation water heights.

We applied the Thornthwaite equation [57] to account for daily rates of potential ET (PET) over each study area. This method was selected instead of the widely used Penman–Monteith equation [58] because it requires only temperature as input. Therefore, it can be easily calculated in the absence of meteorological stations measuring wind speed, humidity and radiation, making it suitable for large-scale analysis. The original formulation by Thornthwaite computes monthly PET (PET_M), for a standard month of 30 days with a fixed 12 h photoperiod, as follows:

$$PET_M = 16\left(10\,\frac{T}{I}\right)^{a} \quad (5)$$

$$I = \sum_{n=1}^{12} (0.2\,T)^{1.514},\ T > 0°C \quad (6)$$

$$a = 6.75{\cdot}10^{-7}I^3 - 7.71{\cdot}10^{-5}I^2 + 1.7912{\cdot}10^{-2}I + 0.49239 \quad (7)$$

where T is the monthly average temperature. Camargo et al. (1999) [59] obtained more accurate results by replacing T with the effective temperature (T_{eff}):

$$T_{eff} = 0.5{\cdot}k\,(3\,T_{max} - T_{min}) \quad (8)$$

with T_{min} and T_{max} denoting the daily minimum and maximum temperature of the month, respectively. Following Pereira and Pruitt (2004) [60], we set k to 0.69 for estimating daily PET (PET_D). Furthermore, to account for the impact of the photoperiod (N), T_{eff} was corrected with the day-night ratio [60] as follows:

$$T^{*}_{eff} = T_{eff}\,\frac{N}{24 - N} \quad (9)$$

N is the number of light hours in a day and is obtained based on the location of the study site and the day of year. Daily potential ET was obtained dividing PET_M by 30. Actual ET is expected to be equal to PET after irrigation, i.e., not limited by soil moisture conditions. As the exact timings of irrigation is unknown, we assumed the irrigation to occur in the middle of two satellite overpasses. Hence, for each detected irrigation event, we calculated the number of days (n_{days}) from the previous Sentinel-1 acquisition, and ET losses were estimated as follows:

$$ET_{loss} = PET_D \frac{n_{days}}{2} \quad (10)$$

3.2.2. Accounting for Drainage

Drainage from the top layer of the soil can be expressed through a power law equation [42,61]:

$$g_t = a \cdot SM_{t-1}^b \quad (11)$$

where a [mm/day] and b [-] are related to soil properties and express the non-linearity between the infiltration rate and the relative soil moisture content. The two parameters were obtained from tabulated values and were set to 621 mm/day and 9.21, for a and b, respectively, according to the soil texture class of the study sites [62,63]. Hence, we expect that differences in the drainage rate among the test sites will not be affected by site-specific soil characteristics. Small variations of soil texture, as in our case, were found to be negligible on the observed saturated hydraulic conductivity [64]. Note that the amount of water drained to deeper soil layers is calculated using the surface soil moisture of the previous satellite acquisition (SM_{t-1}). This formulation was adopted because the actual soil moisture conditions immediately after irrigation are not known. The drainage water loss at each irrigation event was obtained, as above, by multiplying the daily drainage (g_t) with half of the number of days (n_{days}) from the previous satellite acquisition:

$$g_{loss} = g_t \frac{n_{days}}{2} \quad (12)$$

3.3. Evaluation

A detected irrigation event was classified as true positive (TP) if irrigation took place within 5 days before and 1 day after the detected event. Conversely, if irrigation did not occur during this temporal window, the detected event was set as false positive (FP). The temporal window was based on the longest possible overpass time between consecutive Sentinel-1 acquisitions (~5 days). We included a positive shift of one day to account for uncertainties in the reporting of irrigation dates and differences in the timing of irrigation and satellite overpass. For instance, Sentinel-1 observations acquired during the descending orbit (approximately 5 a.m.) cannot detect an irrigation event occurring later in the same day. Only the irrigation date was reported rather than the actual time of the day. The number of detectable irrigation events might be lower than the total number of irrigation events reported by a farmer. If two or more irrigation events occurred between consecutive satellite acquisitions, they have been considered as one event [65]. The number of undetected irrigation events, or false negative (FN), was obtained as difference between detectable events and TP. Finally, precision (p) and recall (r) were calculated as:

$$p = \frac{TP}{TP + FP} \quad (13)$$

$$r = \frac{TP}{TP + FN} \quad (14)$$

Both p and r can vary between 1 and 0 (best and worst case, respectively). The F-score is computed as harmonic mean of precision and recall. Furthermore, we assessed the

agreement between the seasonally cumulated irrigation estimates against the reported data, both qualitatively and quantitatively, in terms of Pearson's correlation coefficient and bias.

4. Results and Discussion

4.1. Selection of Optimal Grid Size

Figure 3 shows the effect of various grid sizes on the calculation of the areal soil moisture increases. ΔSM_{areal}, calculated for n ranging between 5 and 39 pixels, was compared against ΔSM_{local} for each irrigation event, and the skill obtained for the smallest possible surrounding window (n = 3 pixels) was then considered as the baseline to investigate the benefit of using larger spatial windows. Improvements obtained for larger grid sizes compared to the baseline (green dots) suggest that in some cases larger grids do not improve the result, as a plateau is reached (e.g., BB1). In other instances, the differences in soil moisture response between irrigated pixels (fields) and the surroundings (e.g., at the NS site) monotonically increase with larger window sizes for ΔSM_{areal}; hence, no optimal window size could be determined. Furthermore, the mean differences are considerably higher for the BB1 site, and to a lesser extent BB2, compared to NS. These results are the combined effect of various factors, such as the irrigation system and management practices, field sizes and heterogeneity of the surrounding landscape. Indeed, large differences are expected if irrigated fields are surrounded by non-irrigated fields, or at least if irrigation does not occur simultaneously in (most of) the fields within the spatial window used to compute the areal soil moisture. Additionally, distinct soil moisture increases arise from the field-specific irrigation system and/or management practices. For instance, sprinkler vs. drip irrigation, as well as intermittent distribution of large amounts of water vs. frequent irrigation with low volumes, would result in different optimal grid sizes. The marginal differences (orange crosses), i.e., the relative improvement obtained by increasing n compared to the previous grid size, shows consistent trends among the three sites. In fact, marginal differences increased until spatial windows of 11–19 pixels and decrease afterwards. Therefore, we selected n = 15 pixels as the optimal surrounding area for detecting field scale irrigation, and the following analyses are based on this window size.

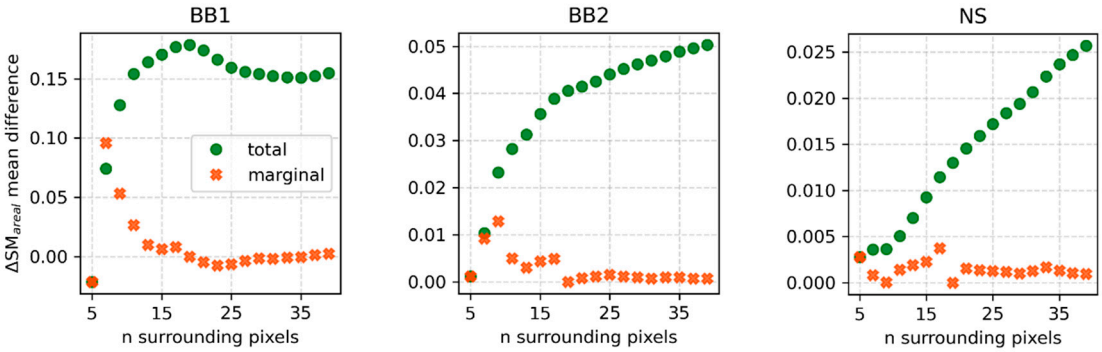

Figure 3. Benefit of employing larger grid sizes to calculate ΔSM_{areal} compared to the smallest possible grid, i.e., n = 3 (green dots), and marginal improvements obtained for grid size n compared to the previous grid size, i.e., $n - 2$ (orange crosses).

4.2. Detection of Irrigation Events

Figure 4 illustrates the ability of the proposed method to detect individual irrigation events depending on the SM_{ratio_t} value employed. The results refer to the irrigation period based on known irrigation dates (IP_{actual}), while the results obtained for $IP_{default}$ and IP_{NDVI} are provided in the Supplementary Materials (Figure S1) and summarized in Table 1. Precision, recall and F-score are grouped by the fraction of irrigated area within S1-SSM pixels. Some differences in the skill to track individual irrigation events among the three sites are visible. For instance, at the BB1 site, both precision and recall were satisfactory with values higher than 0.80 when considering SM_{ratio_t} values smaller than

1.1. Hence, very few of the detected events were false positives, and only a small number of irrigation events remained undetected. Conversely, the recall was rather low at the NS site. The reason for this finding lies in the irrigation management used for most fields at NS, consisting of frequent, often daily, application of small amounts of water. Hence, the irrigation signal might not be visible depending on the amount of water allocated during an irrigation event and the time occurring until the subsequent satellite acquisition [31,41]. This finding indicates that extensive irrigation leads to stronger soil moisture differences between irrigated and rainfed pixels, and therefore to better discrimination of irrigation events.

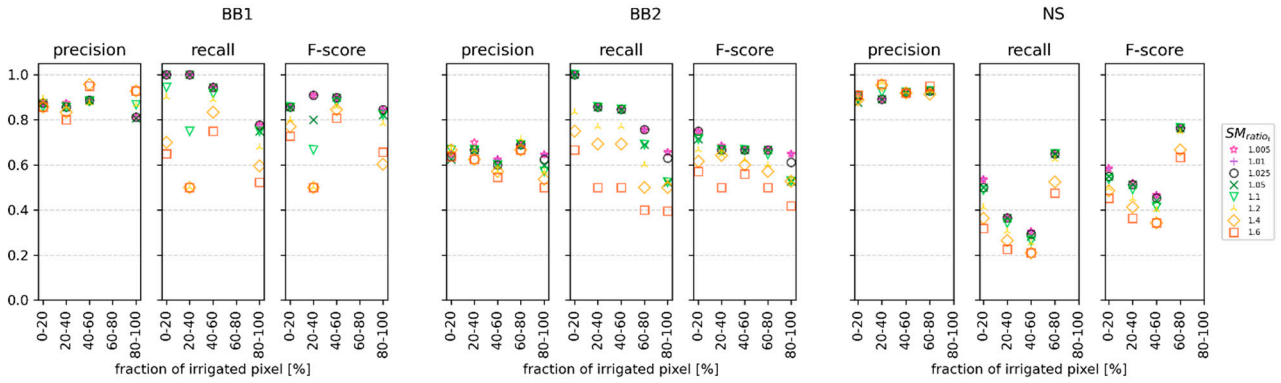

Figure 4. Detection accuracy expressed as precision, recall and F-score, for the irrigation period based on actual irrigation dates reported by farmers (IP_{actual}). The results are grouped by the fraction of irrigated area within S1-SSM pixels.

Contrary to our expectation, the recall did not always improve with improving the fraction of irrigated area covered by S1-SSM pixels (e.g., BB2). This finding can be ascribed to the lower reliability of the S1-SSM product under densely vegetated conditions, as vegetation water content and plant structure are wrongly attributed to soil moisture. Hence, positive biases in the soil moisture retrieval are expected for pixels with high irrigation fractions, likely characterized by more vigorous vegetation [40]. This may mask actual soil moisture dynamics, i.e., drying and wetting. As a result, more irrigation events were not detected, causing the recall to decrease. Similar findings were obtained by Bazzi et al. (2020) [66], who reported that undetected irrigation events occur more frequently for well-developed canopies (NDVI > 0.8). Indeed, C-band SAR was shown to be insensitive to soil moisture for highly developed vegetation cover [67].

Table 1 summarizes the detection accuracy for the different combinations of SM_{ratio_t} values tested and irrigation periods considered. The results are the averages of precision, recall and F-score obtained for the different fractional irrigated groups weighted by the number of pixels belonging to each group (Figure 2). Employing more inclusive, i.e., smaller, values of SM_{ratio_t} provided better recall scores, indicating fewer missed irrigation events. Conversely, the precision was generally higher, even though with smaller gains, if more conservative, i.e., higher, SM_{ratio_t} values were used. The F-score, which accounts for both precision and recall, was consistently higher for SM_{ratio_t} smaller than 1.05, suggesting that more inclusive thresholds provide better detection skill. In particular, the best overall accuracy was found for SM_{ratio_t} equal to 1.01, hence further results on the quantification of irrigation water amounts refer to events detected using this value.

Table 1. Summary of detection accuracy (precision, recall and F-score) depending on the SM_{ratio_t} value employed for discriminating soil moisture increases as irrigation and the irrigation period (IP) considered. The highest F-score for each IP is shown in bold.

Site	IP	Metric	SM_{ratio_t}							
			1.005	**1.01**	**1.025**	**1.05**	**1.1**	**1.2**	**1.4**	**1.6**
BB1	**default**	p	0, 81	0, 81	0, 81	0, 81	0, 80	0, 89	0, 91	0, 90
		r	1, 00	1, 00	1, 00	1, 00	0, 93	0, 85	0, 69	0, 64
		F	**0, 90**	**0, 90**	**0, 90**	0, 89	0, 86	0, 87	0, 79	0, 75
	NDVI	p	0, 37	0, 39	0, 39	0, 41	0, 41	0, 41	0, 44	0, 62
		r	0, 91	0, 91	0, 86	0, 86	0, 74	0, 66	0, 61	0, 55
		F	0, 53	0, 55	0, 54	**0, 56**	0, 53	0, 50	0, 51	0, 58
	actual	p	0, 87	0, 87	0, 86	0, 86	0, 86	0, 88	0, 87	0, 87
		r	0, 98	0, 98	0, 97	0, 96	0, 89	0, 82	0, 67	0, 62
		F	**0, 92**	**0, 92**	0, 91	0, 91	0, 87	0, 85	0, 76	0, 72
BB2	**default**	p	0, 37	0, 37	0, 37	0, 37	0, 37	0, 35	0, 35	0, 39
		r	0, 91	0, 91	0, 90	0, 89	0, 89	0, 86	0, 74	0, 61
		F	0, 52	**0, 53**	**0, 53**	0, 52	0, 52	0, 49	0, 48	0, 48
	NDVI	p	0, 21	0, 21	0, 21	0, 21	0, 22	0, 23	0, 22	0, 24
		r	0, 88	0, 88	0, 88	0, 87	0, 87	0, 76	0, 68	0, 54
		F	0, 34	0, 34	0, 34	0, 34	**0, 35**	**0, 35**	0, 34	0, 33
	actual	p	0, 67	0, 66	0, 64	0, 64	0, 65	0, 65	0, 63	0, 61
		r	0, 88	0, 88	0, 88	0, 87	0, 87	0, 76	0, 68	0, 54
		F	**0, 76**	0, 75	0, 74	0, 74	0, 74	0, 70	0, 65	0, 58
NS	**default**	p	0, 66	0, 66	0, 66	0, 67	0, 68	0, 69	0, 69	0, 75
		r	0, 54	0, 53	0, 52	0, 51	0, 49	0, 42	0, 37	0, 33
		F	**0, 59**	**0, 59**	0, 58	0, 58	0, 57	0, 52	0, 48	0, 46
	NDVI	p	0, 59	0, 59	0, 59	0, 61	0, 61	0, 62	0, 67	0, 67
		r	0, 55	0, 55	0, 53	0, 52	0, 50	0, 47	0, 38	0, 34
		F	**0, 57**	**0, 57**	0, 56	0, 56	0, 55	0, 53	0, 49	0, 45
	actual	p	0, 91	0, 91	0, 91	0, 89	0, 91	0, 91	0, 91	0, 92
		r	0, 48	0, 48	0, 45	0, 45	0, 44	0, 38	0, 33	0, 29
		F	**0, 63**	**0, 63**	0, 60	0, 60	0, 59	0, 53	0, 48	0, 44

The F-score obtained when known irrigation dates were used to constrain the irrigation period (IP_{actual}) outperformed the results obtained for $IP_{default}$ and IP_{NDVI}. Specifically, the latter recorded the lowest scores among the three irrigation periods considered. A possible reason for this outcome is the difficulty to establish a widely applicable relationship between the growing cycle and the irrigation period, as this might strongly vary among different crops [3,44,68]. Furthermore, the definition of IP_{NDVI} employed here might be not well suited for, e.g., sequential cropping patterns characterized by winter cereals followed by summer crops, as found in many fields at BB2 site. The irrigation detection considering IP_{NDVI}, and to a lesser extent $IP_{default}$, was skewed for these fields, with irrigation events identified before the actual start of the summer crop cycle, i.e., either wrongly attributed rainfall or irrigation occurred during the last stages of the winter crops. Indeed, the F-score increased from 0.34 (0.53) to 0.75 from considering the IP_{NDVI} ($IP_{default}$) to IP_{actual}. In line with López Valencia et al. (2020) [69], we conclude that a correct definition of the start and end of season is critical to higher detection accuracy.

Le Page et al. (2020) [70] analyzed the detection of irrigation events over six fields in France using the S^2MP product [56] and reported F-scores ranging between 0.31 and 0.80 (average 0.69). Notwithstanding the benefit of monitoring soil moisture on a field scale, hence avoiding the presence of mixed pixels (i.e., S^2MP), we obtained comparable results. However, S^2MP is (currently) only available for few selected sites (https://www.theia-land.fr/en/product/soil-moisture-with-very-high-spatial-resolution/, accessed on

24 February 2021), while the S1-SSM product is generated for the entire Europe. Bazzi et al. (2020) [65] developed a decision tree method based on Sentinel-1 backscatter observations to detect irrigation events at the plot scale and to further discriminate between irrigated and rainfed fields. With their approach, the authors were able to correctly identify 84% of the irrigation events, i.e., precision, over three plots in Montpellier (South-east France). These results are similar to those observed in our study considering IP_{actual}, i.e., precision equal to 0.87, 0.66 and 0.91 for the three sites tested.

Overall, the ability to detect individual events was very satisfactory over the three sites (F-score of 0.92, 0.75 and 0.63 for the BB1, BB2 and NS sites, respectively) employing IP_{actual}, and only slightly lower considering $IP_{default}$ (0.90, 0.53 and 0.59). Hence, our findings suggest that most of the irrigation events occurring in a field can be detected and discerned from precipitation using the TU Wien S1-SSM product with 500 m sampling and 1.5–4 days temporal resolution.

4.3. Quantification of Irrigation Water Amounts

Figure 5 depicts the median values of the irrigation amounts retrieved throughout the growing season for each pixel, grouped by the fraction of irrigated area within each pixel. Differences between the NS and the BB sites are consistent with the information reported by farmers. All fields at both BB locations were equipped with center pivot systems and were generally characterized by higher irrigation volumes per event compared to the NS site. Most of the BB fields were subject to a limited number of (temporally) distinct irrigation events, each characterized by extensive water distribution. Conversely, most fields at the NS site underwent numerous irrigation events with smaller amounts of water distributed. The diversity in irrigation practices is clearly reflected in Figure 5, where the estimated irrigation at the NS site is systematically lower compared to both BB1 and BB2 sites. Furthermore, the estimated irrigation was found to increase with increasing the fraction of irrigated pixel. Indeed, higher irrigation amounts are expected over largely irrigated pixels, at least given identical irrigation system and similar management practices. Overall, these findings indicate that the proposed algorithm can effectively retrieve irrigation heights regardless of field-specific features, i.e., distinct irrigation systems and management practices.

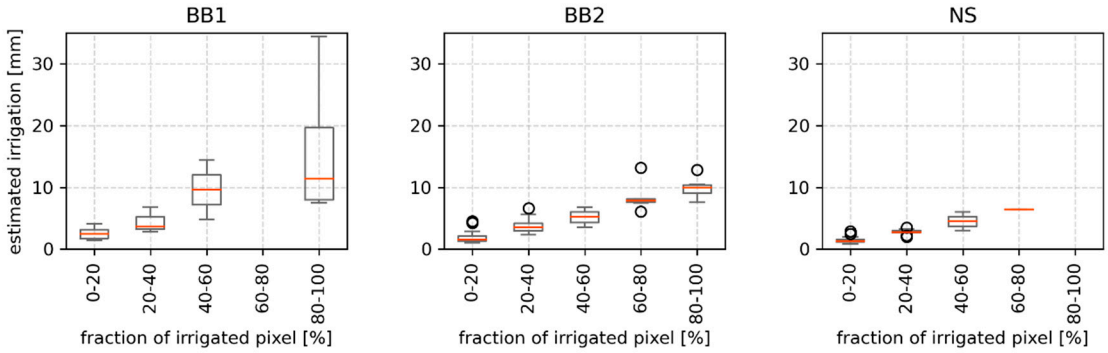

Figure 5. Median irrigation heights of individual events estimated for each pixel throughout the irrigation period, grouped by the fraction of pixel irrigated.

For each irrigation event, we further differentiated the contribution to the total irrigation water height coming from ΔSM, ET and g (Figure 6). Overall, we found that ET was predominant compared to ΔSM and g in accordance with Dari et al. (2020) [71]. The average ET contribution over the three test sites varied between 45% and 66% of the total, while the contribution of soil moisture variation ranged between 21% and 33%. Similar to Jalilvand et al. (2019) [33], the drainage term was in most cases negligible (median = 0); however, some peaks occurred, especially at the BB1 and BB2 sites. This finding can be ascribed to two main drivers: the lack of a dynamic vegetation correction in the S1-SSM retrieval algorithm and the (occasionally) long time between consecutive satellite

acquisitions. Because of the first factor, i.e., vegetation changes are not accounted for in the retrieval, soil moisture was overestimated for pixels with very dense and vigorous vegetation. As drainage is proportionally related to soil moisture, positively biased soil moisture would lead to overestimated drainage rates (see Equation (11)). Similarly, the amount of water lost through drainage increases with increasing time between two consecutive satellite overpasses (see Equation (12)). The average Sentinel-1 temporal resolution over the study sites was of approximately 1.5–2 days; however, a few long gaps (>8 days) were found for the BB1 site and to a lesser extent for the BB2 site. Obviously, if both factors, i.e., positively biased soil moisture and long gaps between satellite acquisitions, occurred simultaneously, the estimated drainage losses were distorted and not representative of actual conditions.

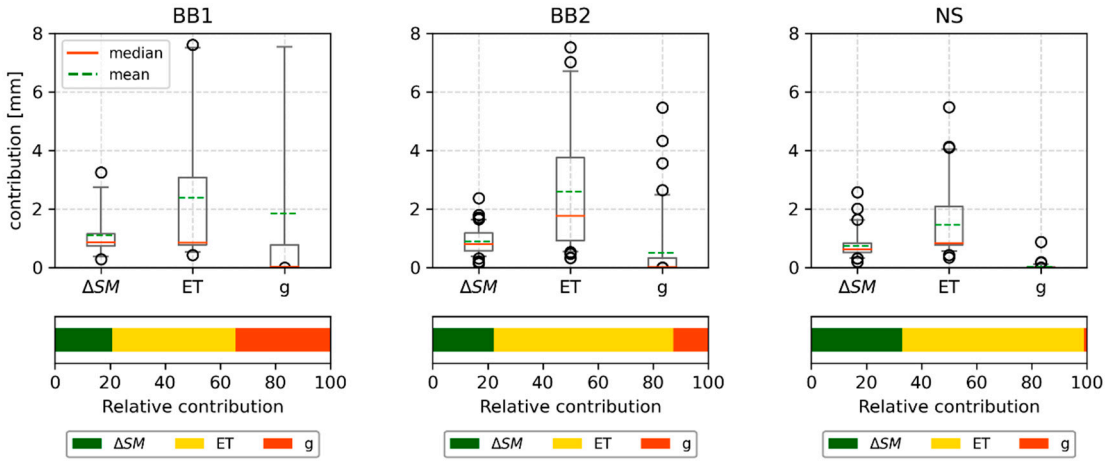

Figure 6. Contribution to the estimated irrigation water height for all individual events coming from the following components: soil moisture increase between consecutive overpasses (ΔSM), evapotranspiration (ET) and drainage (g). Bar plots show the mean relative contribution.

Figure 7 shows time series of spatially aggregated irrigation heights, both estimated and reported by farmers, aggregated to a weekly interval. The irrigation dynamics estimated for the BB1 site correspond well with the reference data. However, irrigation was significantly overestimated in June, mostly due to drainage, as shown in Figure 6. At the BB2 site, only a moderate agreement between the reported and estimated irrigation heights was found. Most notably, large underestimations can be observed at the beginning (April–May) and end (August–September) of the growing season. A possible explanation for this result can be attributed to the overall wetter conditions found during both periods, driven by abundant precipitation. Additionally, a pronounced drop in estimated irrigation is visible around mid-July. After a close inspection of the S1-SSM data, we found that (on average) more than 14 acquisitions per month were available for this location during the period May–October 2019. However, in July, there were fewer than 12 observations, resulting in a lower temporal resolution. As shown in Figure 4, the recall score for the BB2 site worsened, i.e., more events were missed, for pixels with a large irrigation fraction. As a result, the retrieved irrigation water heights for such pixels were greatly underestimated, leading to the observed drop in the spatially averaged irrigation time series. We found good agreement between reported and estimated irrigation dynamics at the NS site; however, the magnitude of the retrieved irrigation was significantly lower. This outcome stems from the numerous missed irrigation events, as reflected by the low recall (Figure 4), due to the irrigation management employed across most fields at the NS site. Besides, only one irrigation event was assumed to take place within two consecutive satellite acquisitions, which was defined to occur in the middle (see Equation (10)). However, this was often not the case for most fields at the NS site, where daily irrigation could sustain higher ET rates, leading to considerably higher ET losses than estimated (Figure 6). Overall, irrigation

dynamics were captured moderately well, and discrepancies with reference data were largely the result of inherent S1-SSM characteristics (e.g., lack of vegetation correction and revisit time).

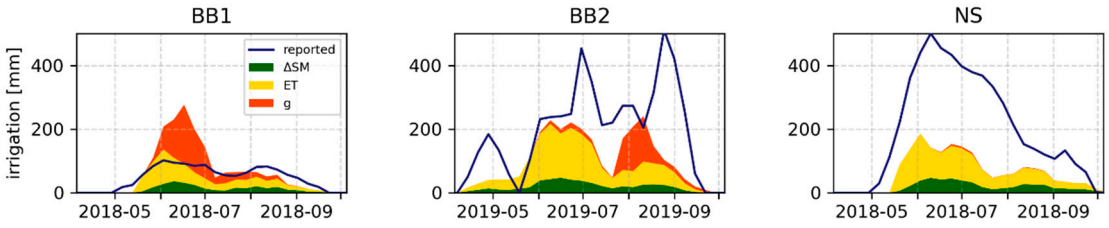

Figure 7. Time series of spatially cumulated irrigation water heights, aggregated on a weekly basis. Estimated irrigation, with the explicit contribution of each term to the total, is compared against reference data reported by farmers.

We further evaluated the agreement between reported and estimated cumulative irrigation water heights throughout the growing season for all irrigated pixels (Figure 8). Note that results refer to irrigation events detected considering the irrigation period based on known irrigation dates (IP_{actual}). At the BB1 site, we found Pearson's correlation equal to 0.75 and a small positive bias (8 mm), indicating that the retrieved irrigation was slightly overestimated, mostly because of the high drainage contribution (as highlighted in Figures 6 and 7). Such an overestimation could also be the result of the approximate reference irrigation data reported for BB1, i.e., no exact measurements were available. Conversely, BB2 and even more prominently NS are characterized by negative biases (−50 and −98 mm, respectively), denoting an underestimation of the retrieved irrigation heights. Nonetheless, good correlation values were found (0.73 and 0.44 for BB2 and NS, respectively). The results obtained for $IP_{default}$ and IP_{NDVI} show similar trends as IP_{actual} with respect to the three test sites; however, slightly lower agreement was found against the reference data (Figure S2). It should be noted, however, that the present method only accounts for the irrigation water entering the soil. The irrigation efficiency, i.e., water losses due to leakage, wind drift and canopy interception, which is specific for the irrigation system and the environmental conditions at the time of irrigation [72], is not considered.

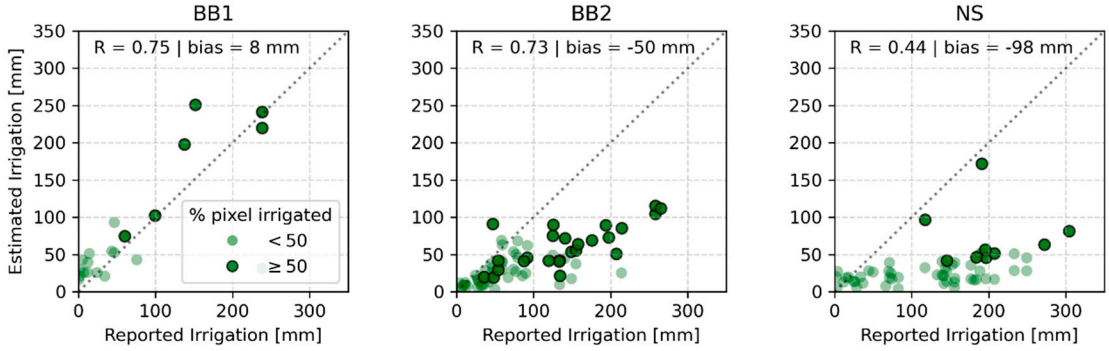

Figure 8. Pixel by pixel comparison of cumulative irrigation water heights between estimated and reference data. S1-SSM pixels with a fractional irrigation area higher than 50% are highlighted.

These results are in line with those of Dari et al. (2020) [71], who found Pearson coefficient ranging between 0.58 and 0.81, and biases from −337 to 80 mm. Other studies based on coarse resolution soil moisture products reported lower accuracies between reference and estimated irrigation water heights [35], while Jalilvand et al. (2019) [33] found high correlation (0.86) over few largely irrigated pixels in a semi-arid region after accounting for biases. Finally, no differences in the skill of the proposed irrigation retrieval approach were found depending on the cultivated crop, suggesting that it could be effectively employed over a wide range of crop types.

4.4. Improvements and Transferability

The irrigation retrieval proposed in this study proved adequately accurate; nevertheless, additional refinements could be directed to the estimation of drainage and evapotranspiration. For instance, the modified version of the Thornthwaite equation employed in this analysis could be further refined by applying a linear interpolation between monthly estimates of potential ET, ensuring smoother daily dynamics. Furthermore, the Thornthwaite equation, chosen to guarantee its applicability even in the absence of meteorological stations, could be replaced when such information is available by, e.g., the Penman–Monteith approach [58]. Alternatively, remotely sensed or model-based estimates of either potential or actual ET could be employed, such as products from MODIS [73,74] or ERA5-Land [75]. To minimize the negative effect of the occasionally long satellite revisit time on the estimation of both g and ET, a maximum threshold of three days between consecutive acquisitions could be introduced [31]. It should also be highlighted that the amplitude of the estimated irrigation water amounts is strongly related to the accuracy of the soil porosity data used to convert soil moisture from saturation degrees to volumetric content.

Employing the TU Wien Sentinel-1 Surface Soil Moisture [40] product yielded promising results for both the detection and quantification of irrigation at 500 m. It is worth emphasizing, however, that the lack of a dynamic vegetation correction module in the retrieval algorithm was seemingly the main cause of poor detection accuracy during the peak of the growing season. In addition, the drainage term was, in a few instances, largely overestimated because of soil moisture values close to saturation originated by the effect of vegetation on backscatter. Hence, a vegetation correction module in the retrieval algorithm is expected to greatly improve the performance of the S1-SSM product [40], and consequently our results for both the detection and the quantification of irrigation.

Currently, the framework presented in this study could be applied to entire continental Europe. The results presented in this study highlight the importance of correctly defining the irrigation period. The IP_{actual} scenario was included to show the accuracy potentially achievable in an ideal case; however, alternative methods need to be developed to obtain reliable irrigation periods in more realistic settings, e.g., for irrigation retrieval at regional (or continental) scale. For offline analysis, this could be achieved by inferring the dominant crop within each pixel [76–80], and subsequently deriving irrigation time windows based on the specific combination of crop type and location (i.e., meteorological and environmental characteristics). In a real-time application, proxies of vegetation development represent the best solution to infer such an irrigation period. Here, we selected NDVI, but recent studies have shown the great potential of using the Sentinel-1 backscatter (e.g., cross-ratio) as an alternative to optical sensors [81–85]. Furthermore, the application of this framework over large areas would require an accurate identification of irrigated fields in order to narrow the irrigation retrieval only to those pixels, hence using spatially detailed maps of irrigated fields (e.g., [86,87]).

Notwithstanding the applicability of the proposed method at the continental scale, it is worth emphasizing that the effectiveness of the irrigation detection and quantification will depend on a number of different factors, including the satellite revisit time, irrigation system and management and fractional coverage of irrigated fields. Precise retrievals can be expected for pixels (and regions) characterized by good Sentinel-1 temporal coverage, i.e., shorter than three days. The launch of the new Sentinel-1 C, planned for 2022 [88], would lead to considerable increase of the temporal resolution, hence improving the overall skill of the approach. Additionally, the method presented in this work is expected to be more sensitive to irrigation systems characterized by low efficiency, such as gravity and sprinkler irrigation, as the irrigation signal due to soil wetting is more pronounced in the retrieved soil moisture [35]. Furthermore, both field size and field coverage by satellite pixels are crucial factors for successful detection and quantification tasks. In fact, the irrigation signal coming from small fields (<<25 ha) will be mixed, and possibly masked, by the surrounding features observed by the same satellite pixel. In addition, large irrigated

fields (≥25 ha) can be subject to the same issue if covered by various satellite pixels, i.e., depending on the satellite sensor observation geometry. This issue could be addressed by testing downscaled SSM products [37,89] available at sub-field scale.

5. Conclusions

We present a novel methodology harnessing the spatial and temporal patterns of the TU Wien Sentinel-1 Surface Soil Moisture product for the detection and quantification of irrigation at 500 m sampling. Disentangling the effect of field-scale irrigation on the retrieved soil moisture is not straightforward, as the latter is affected by various other factors. The irrigation retrieval includes formulations of drainage and evapotranspiration losses because of their considerable impact on soil moisture variations at sub-daily time scales. One of the key advantages of this method compared to other approaches based on microwave soil moisture data is that it does not rely on additional datasets, which either are available over large scales but only at coarse resolution or exist at (sub-)kilometric resolution but only at the catchment or regional scale. We quantitatively assessed the proposed methodology against irrigation data provided by farmers at three sites with distinct characteristics in terms of cultivated crops, field size and irrigation system, allowing a thorough investigation of strengths and limitations of the approach. Specifically, we are able to draw the following conclusions:

- A correct definition of the irrigation period (typically only a subset of the whole year) is crucial as it leads to better discrimination of individual events.
- Simple formulations of evapotranspiration and drainage improved the irrigation estimates while ensuring the applicability to large regions and locations without meteorological stations. More sophisticated representations of these processes are expected to further improve the irrigation retrievals.
- The proposed approach can provide accurate irrigation estimates at a spatial resolution of 500 m regardless of field-specific characteristics (e.g., crop type).

Notwithstanding uncertainties in the estimated irrigation water amounts, we were able to provide valuable information about spatial patterns and temporal dynamics of irrigation at unprecedented scales. Hence, the method presented here has the great potential to contribute to a better monitoring of irrigation trends, in both space and time, at quasi-field scale. Future work will be directed towards improving the formulations of evapotranspiration and drainage, as well as replacing NDVI with Sentinel-1-derived vegetation proxies (i.e., cross ratio). Furthermore, the analysis will be extended to larger (e.g., country) scales.

Supplementary Materials: The following are available online at https://www.mdpi.com/article/10.3390/rs13091727/s1, Figure S1: Detection accuracy expressed as precision, recall and F-score, for the irrigation period based on: (a) default dates; and (b) NDVI-derived phenology. Figure S2: Pixel by pixel comparison of cumulative irrigation water heights between estimated and reference data for the irrigation period based on: (a) default dates; and (b) NDVI-derived phenology.

Author Contributions: Conceptualization and methodology, L.Z., S.S. and W.D.; reference data provision, C.N. and B.Z.; generation of S1-SSM data, B.B.-M.; formal analysis, L.Z.; writing—original draft preparation, L.Z.; and writing—review and editing, S.S., B.B.-M., C.N., B.Z. and W.D. All authors have read and agreed to the published version of the manuscript.

Funding: This research was funded by the European Space Agency (ESA) through the IRRIGATION+ project (contract number 4000129870/20/I-NB) and the Austrian Research Promotion Agency (FFG) via the DWC-Radar project (project number 873658). Open Access Funding by TU Wien.

Data Availability Statement: Not applicable.

Acknowledgments: The authors acknowledge TU Wien Bibliothek for financial support through its Open 500 Access Funding Program.

Conflicts of Interest: The authors declare no conflict of interest.

References

1. Foley, J.; Prentice, C.; Ramankutty, N.; Levis, S.; Pollard, D.; Sitch, S.; Haxeltine, A. An Integrated Biosphere Model of Land Surface Processes, Terrestrial Carbon Balance, and Vegetation Dynamics. *Glob. Biogeochem. Cycles* **1996**, *10*, 603–628. [CrossRef]
2. United Nations Educational. *World Water Assessment & Water*; Water in a Changing World; UNESCO: Paris, France, 2009.
3. Siebert, S.; Döll, P. Quantifying Blue and Green Virtual Water Contents in Global Crop Production as Well as Potential Production Losses without Irrigation. *J. Hydrol.* **2010**, *384*, 198–217. [CrossRef]
4. Foley, J.A.; Ramankutty, N.; Brauman, K.A.; Cassidy, E.S.; Gerber, J.S.; Johnston, M.; Mueller, N.D.; O'Connell, C.; Ray, D.K.; West, P.C.; et al. Solutions for a Cultivated Planet. *Nature* **2011**, *478*, 337–342. [CrossRef]
5. Shiklomanov, I.A. Appraisal and Assessment of World Water Resources. *Water Int.* **2000**, *25*, 11–32. [CrossRef]
6. Famiglietti, J.S. The Global Groundwater Crisis. *Nat. Clim. Chang.* **2014**, *4*, 945–948. [CrossRef]
7. Wada, Y.; van Beek, L.P.H.; Bierkens, M.F.P. Nonsustainable Groundwater Sustaining Irrigation: A Global Assessment: Nonsustainable Groundwater Sustaining Irrigation. *Water Resour. Res.* **2012**, *48*. [CrossRef]
8. Amezketa, E. An Integrated Methodology for Assessing Soil Salinization, a Pre-Condition for Land Desertification. *J. Arid Environ.* **2006**, *67*, 594–606. [CrossRef]
9. Chaudhuri, S.; Roy, M. Irrigation Water Pricing in India as a Means to Conserve Water Resources: Challenges and Potential Future Opportunities. *Environ. Conserv.* **2019**, *46*, 99–102. [CrossRef]
10. Deng, J.; Guo, L.; Salas, W.; Ingraham, P.; Charrier-Klobas, J.G.; Frolking, S.; Li, C. Changes in Irrigation Practices Likely Mitigate Nitrous Oxide Emissions from California Cropland. *Glob. Biogeochem. Cycles* **2018**, *32*, 1514–1527. [CrossRef]
11. Cook, B.I.; Shukla, S.P.; Puma, M.J.; Nazarenko, L.S. Irrigation as an Historical Climate Forcing. *Clim. Dyn.* **2015**, *44*, 1715–1730. [CrossRef]
12. Sacks, W.J.; Cook, B.I.; Buenning, N.; Levis, S.; Helkowski, J.H. Effects of Global Irrigation on the Near-Surface Climate. *Clim. Dyn.* **2009**, *33*, 159–175. [CrossRef]
13. Gormley-Gallagher, A.M.; Sterl, S.; Hirsch, A.L.; Seneviratne, S.I.; Davin, E.L.; Thiery, W. Agricultural Management Effects on Mean and Extreme Temperature Trends. *Earth Syst. Dynam. Discuss.* **2020**. [CrossRef]
14. Kueppers, L.M.; Snyder, M.A.; Sloan, L.C. Irrigation Cooling Effect: Regional Climate Forcing by Land-Use Change. *Geophys. Res. Lett.* **2007**, *34*, L03703. [CrossRef]
15. Eekhout, J.P.C.; Hunink, J.E.; Terink, W.; de Vente, J. Why Increased Extreme Precipitation under Climate Change Negatively Affects Water Security. *Hydrol. Earth Syst. Sci.* **2018**, *22*, 5935–5946. [CrossRef]
16. Kummu, M.; Guillaume, J.H.A.; de Moel, H.; Eisner, S.; Flörke, M.; Porkka, M.; Siebert, S.; Veldkamp, T.I.E.; Ward, P.J. The World's Road to Water Scarcity: Shortage and Stress in the 20th Century and Pathways towards Sustainability. *Sci. Rep.* **2016**, *6*, 38495. [CrossRef] [PubMed]
17. Rockström, J.; Falkenmark, M.; Lannerstad, M.; Karlberg, L. The Planetary Water Drama: Dual Task of Feeding Humanity and Curbing Climate Change: Frontier. *Geophys. Res. Lett.* **2012**, *39*. [CrossRef]
18. Vorosmarty, C.J. Global Water Resources: Vulnerability from Climate Change and Population Growth. *Science* **2000**, *289*, 284–288. [CrossRef] [PubMed]
19. Ray, D.K.; Mueller, N.D.; West, P.C.; Foley, J.A. Yield Trends Are Insufficient to Double Global Crop Production by 2050. *PLoS ONE* **2013**, *8*, e66428. [CrossRef] [PubMed]
20. Deines, J.M.; Kendall, A.D.; Hyndman, D.W. Annual Irrigation Dynamics in the U.S. Northern High Plains Derived from Landsat Satellite Data: Satellite-Derived Irrigation Dynamics. *Geophys. Res. Lett.* **2017**, *44*, 9350–9360. [CrossRef]
21. Siebert, S.; Doll, P.; Hoogeveen, J. Development and Validation of the Global Map of Irrigation Areas. *Hydrol. Earth Syst. Sci.* **2005**, *9*, 535–547. [CrossRef]
22. Novo, P.; Dumont, A.; Willaarts, B.A.; López-Gunn, E. More Cash and Jobs per Illegal Drop? The Legal and Illegal Water Footprint of the Western Mancha Aquifer (Spain). *Environ. Sci. Policy* **2015**, *51*, 256–266. [CrossRef]
23. Foster, T.; Mieno, T.; Brozović, N. Satellite-Based Monitoring of Irrigation Water Use: Assessing Measurement Errors and Their Implications for Agricultural Water Management Policy. *Water Resour. Res.* **2020**, *56*. [CrossRef]
24. Maselli, F.; Battista, P.; Chiesi, M.; Rapi, B.; Angeli, L.; Fibbi, L.; Magno, R.; Gozzini, B. Use of Sentinel-2 MSI Data to Monitor Crop Irrigation in Mediterranean Areas. *Int. J. Appl. Earth Obs. Geoinf.* **2020**, *93*, 102216. [CrossRef]
25. Vanino, S.; Nino, P.; De Michele, C.; Falanga Bolognesi, S.; D'Urso, G.; Di Bene, C.; Pennelli, B.; Vuolo, F.; Farina, R.; Pulighe, G.; et al. Capability of Sentinel-2 Data for Estimating Maximum Evapotranspiration and Irrigation Requirements for Tomato Crop in Central Italy. *Remote Sens. Environ.* **2018**, *215*, 452–470. [CrossRef]
26. Droogers, P.; Immerzeel, W.W.; Lorite, I.J. Estimating Actual Irrigation Application by Remotely Sensed Evapotranspiration Observations. *Agric. Water Manag.* **2010**, *97*, 1351–1359. [CrossRef]
27. Senay, G.; Budde, M.; Verdin, J.; Melesse, A. A Coupled Remote Sensing and Simplified Surface Energy Balance Approach to Estimate Actual Evapotranspiration from Irrigated Fields. *Sensors* **2007**, *7*, 979–1000. [CrossRef]
28. van Dijk, A.I.J.M.; Schellekens, J.; Yebra, M.; Beck, H.E.; Renzullo, L.J.; Weerts, A.; Donchyts, G. Global 5 Km Resolution Estimates of Secondary Evaporation Including Irrigation through Satellite Data Assimilation. *Hydrol. Earth Syst. Sci.* **2018**, *22*, 4959–4980. [CrossRef]
29. Koch, J.; Zhang, W.; Martinsen, G.; He, X.; Stisen, S. Estimating Net Irrigation Across the North China Plain Through Dual Modeling of Evapotranspiration. *Water Resour. Res.* **2020**, *56*. [CrossRef]

30. Khanal, S.; Fulton, J.; Shearer, S. An Overview of Current and Potential Applications of Thermal Remote Sensing in Precision Agriculture. *Comput. Electron. Agric.* **2017**, *139*. [CrossRef]
31. Filippucci, P.; Tarpanelli, A.; Massari, C.; Serafini, A.; Strati, V.; Alberi, M.; Raptis, K.G.C.; Mantovani, F.; Brocca, L. Soil Moisture as a Potential Variable for Tracking and Quantifying Irrigation: A Case Study with Proximal Gamma-Ray Spectroscopy Data. *Adv. Water Resour.* **2020**, *136*, 103502. [CrossRef]
32. Brocca, L.; Tarpanelli, A.; Filippucci, P.; Dorigo, W.; Zaussinger, F.; Gruber, A.; Fernández-Prieto, D. How Much Water Is Used for Irrigation? A New Approach Exploiting Coarse Resolution Satellite Soil Moisture Products. *Int. J. Appl. Earth Obs. Geoinf.* **2018**, *73*, 752–766. [CrossRef]
33. Jalilvand, E.; Tajrishy, M.; Ghazi Zadeh Hashemi, S.A.; Brocca, L. Quantification of Irrigation Water Using Remote Sensing of Soil Moisture in a Semi-Arid Region. *Remote Sens. Environ.* **2019**, *231*, 111226. [CrossRef]
34. Kumar, S.V.; Peters-Lidard, C.D.; Santanello, J.A.; Reichle, R.H.; Draper, C.S.; Koster, R.D.; Nearing, G.; Jasinski, M.F. Evaluating the Utility of Satellite Soil Moisture Retrievals over Irrigated Areas and the Ability of Land Data Assimilation Methods to Correct for Unmodeled Processes. *Hydrol. Earth Syst. Sci.* **2015**, *19*, 4463–4478. [CrossRef]
35. Zaussinger, F.; Dorigo, W.; Gruber, A.; Tarpanelli, A.; Filippucci, P.; Brocca, L. Estimating Irrigation Water Use over the Contiguous United States by Combining Satellite and Reanalysis Soil Moisture Data. *Hydrol. Earth Syst. Sci.* **2019**, *23*, 897–923. [CrossRef]
36. Zohaib, M.; Choi, M. Satellite-Based Global-Scale Irrigation Water Use and Its Contemporary Trends. *Sci. Total Environ.* **2020**, *714*, 136719. [CrossRef] [PubMed]
37. Zappa, L.; Forkel, M.; Xaver, A.; Dorigo, W. Deriving Field Scale Soil Moisture from Satellite Observations and Ground Measurements in a Hilly Agricultural Region. *Remote Sens.* **2019**, *11*, 2596. [CrossRef]
38. Geudtner, D.; Torres, R.; Snoeij, P.; Davidson, M.; Rommen, B. Sentinel-1 System Capabilities and Applications. In Proceedings of the 2014 IEEE Geoscience and Remote Sensing Symposium, Quebec City, QC, Canada, 13–18 July 2014; pp. 1457–1460.
39. Panetti, A.; Rostan, F.; L'Abbate, M.; Bruno, C.; Bauleo, A.; Catalano, T.; Cotogni, M.; Galvagni, L.; Pietropaolo, A.; Taini, G.; et al. Copernicus Sentinel-1 Satellite and C-SAR Instrument. In Proceedings of the 2014 IEEE Geoscience and Remote Sensing Symposium, Quebec City, QC, Canada, 13–18 July 2014; pp. 1461–1464.
40. Bauer-Marschallinger, B.; Freeman, V.; Cao, S.; Paulik, C.; Schaufler, S.; Stachl, T.; Modanesi, S.; Massari, C.; Ciabatta, L.; Brocca, L.; et al. Toward Global Soil Moisture Monitoring with Sentinel-1: Harnessing Assets and Overcoming Obstacles. *IEEE Trans. Geosci. Remote Sens.* **2019**, *57*, 520–539. [CrossRef]
41. Bazzi, H.; Baghdadi, N.; El Hajj, M.; Zribi, M. Potential of Sentinel-1 Surface Soil Moisture Product for Detecting Heavy Rainfall in the South of France. *Sensors* **2019**, *19*, 802. [CrossRef]
42. Brocca, L.; Ciabatta, L.; Massari, C.; Moramarco, T.; Hahn, S.; Hasenauer, S.; Kidd, R.; Dorigo, W.; Wagner, W.; Levizzani, V. Soil as a Natural Rain Gauge: Estimating Global Rainfall from Satellite Soil Moisture Data: Using the Soil as a Natural Raingauge. *J. Geophys. Res. Atmos.* **2014**, *119*, 5128–5141. [CrossRef]
43. Frei, C.; Christensen, J.H.; Déqué, M.; Jacob, D.; Jones, R.G.; Vidale, P.L. Daily Precipitation Statistics in Regional Climate Models: Evaluation and Intercomparison for the European Alps: Daily Precipitation Statistics in Regional Climate Models. *J. Geophys. Res. Atmos.* **2003**, *108*. [CrossRef]
44. Koch, J.; Cornelissen, T.; Fang, Z.; Bogena, H.; Diekkrüger, B.; Kollet, S.; Stisen, S. Inter-Comparison of Three Distributed Hydrological Models with Respect to Seasonal Variability of Soil Moisture Patterns at a Small Forested Catchment. *J. Hydrol.* **2016**, *533*, 234–249. [CrossRef]
45. Shao, Y.; Henderson-Sellers, A. Modeling Soil Moisture: A Project for Intercomparison of Land Surface Parameterization Schemes Phase 2(b). *J. Geophys. Res. Atmos.* **1996**, *101*, 7227–7250. [CrossRef]
46. Rubel, F.; Brugger, K.; Haslinger, K.; Auer, I. The Climate of the European Alps: Shift of Very High Resolution Köppen-Geiger Climate Zones 1800–2100. *Meteorol. Z.* **2017**, *26*, 115–125. [CrossRef]
47. Hengl, T.; Mendes de Jesus, J.; Heuvelink, G.B.M.; Ruiperez Gonzalez, M.; Kilibarda, M.; Blagotić, A.; Shangguan, W.; Wright, M.N.; Geng, X.; Bauer-Marschallinger, B.; et al. SoilGrids250m: Global Gridded Soil Information Based on Machine Learning. *PLoS ONE* **2017**, *12*, e0169748. [CrossRef]
48. Ballabio, C.; Panagos, P.; Monatanarella, L. Mapping Topsoil Physical Properties at European Scale Using the LUCAS Database. *Geoderma* **2016**, *261*, 110–123. [CrossRef]
49. Bauer-Marschallinger, B.; Sabel, D.; Wagner, W. Optimisation of Global Grids for High-Resolution Remote Sensing Data. *Comput. Geosci.* **2014**, *72*, 84–93. [CrossRef]
50. CORINE Land Cover—CLC 2018. Available online: https://land.copernicus.eu/pan-european/corine-land-cover/clc2018 (accessed on 24 February 2021).
51. Al-Yaari, A.; Wigneron, J.-P.; Dorigo, W.; Colliander, A.; Pellarin, T.; Hahn, S.; Mialon, A.; Richaume, P.; Fernandez-Moran, R.; Fan, L.; et al. Assessment and Inter-Comparison of Recently Developed/Reprocessed Microwave Satellite Soil Moisture Products Using ISMN Ground-Based Measurements. *Remote Sens. Environ.* **2019**, *224*, 289–303. [CrossRef]
52. Saxton, K.E.; Rawls, W.J. Soil Water Characteristic Estimates by Texture and Organic Matter for Hydrologic Solutions. *Soil Sci. Soc. Am. J.* **2006**, *70*, 1569–1578. [CrossRef]
53. Riediger, J.; Breckling, B.; Svoboda, N.; Schröder, W. Modelling Regional Variability of Irrigation Requirements Due to Climate Change in Northern Germany. *Sci. Total Environ.* **2016**, *541*, 329–340. [CrossRef] [PubMed]

54. Atzberger, C.; Klisch, A.; Mattiuzzi, M.; Vuolo, F. Phenological Metrics Derived over the European Continent from NDVI3g Data and MODIS Time Series. *Remote Sens.* **2013**, *6*, 257–284. [CrossRef]
55. Beck, H.E.; Vergopolan, N.; Pan, M.; Levizzani, V.; van Dijk, A.I.J.M.; Weedon, G.P.; Brocca, L.; Pappenberger, F.; Huffman, G.J.; Wood, E.F. Global-Scale Evaluation of 22 Precipitation Datasets Using Gauge Observations and Hydrological Modeling. *Hydrol. Earth Syst. Sci.* **2017**, *21*, 6201–6217. [CrossRef]
56. El Hajj, M.; Baghdadi, N.; Zribi, M.; Bazzi, H. Synergic Use of Sentinel-1 and Sentinel-2 Images for Operational Soil Moisture Mapping at High Spatial Resolution over Agricultural Areas. *Remote Sens.* **2017**, *9*, 1292. [CrossRef]
57. Thornthwaite, C.W. An Approach toward a Rational Classification of Climate. *Geogr. Rev.* **1948**, *38*, 55–94. [CrossRef]
58. Monteith, J.L. Evaporation and Environment. *Symp. Soc. Exp. Biol.* **1965**, *19*, 205–234. [PubMed]
59. Camargo, A.P.; Marin, F.R.; Sentelhas, P.C.; Picini, A.G. Adjust of the Thornthwaite's Method to Estimate the Potential Evapotranspiration for Arid and Superhumid Climates, Based on Daily Temperature Amplitude. *Rev. Bras. Agrometeorol.* **1999**, *7*, 251–257.
60. Pereira, A.R.; Pruitt, W.O. Adaptation of the Thornthwaite Scheme for Estimating Daily Reference Evapotranspiration. *Agric. Water Manag.* **2004**, *66*, 251–257. [CrossRef]
61. Famiglietti, J.S.; Wood, E.F. Multiscale Modeling of Spatially Variable Water and Energy Balance Processes. *Water Resour. Res.* **1994**, *30*, 3061–3078. [CrossRef]
62. Brocca, L.; Ciabatta, L.; Moramarco, T.; Ponziani, F.; Berni, N.; Wagner, W. Use of Satellite Soil Moisture Products for the Operational Mitigation of Landslides Risk in Central Italy. In *Satellite Soil Moisture Retrieval*; Elsevier: Amsterdam, The Netherlands, 2016; pp. 231–247. ISBN 978-0-12-803388-3.
63. Rawls, W.J.; Brakensiek, D.L.; Saxton, K.E. Estimation of Soil Water Properties. *Trans. ASAE* **1982**, *25*, 1316–1320. [CrossRef]
64. Picciafuoco, T.; Morbidelli, R.; Flammini, A.; Saltalippi, C.; Corradini, C.; Strauss, P.; Blöschl, G. On the Estimation of Spatially Representative Plot Scale Saturated Hydraulic Conductivity in an Agricultural Setting. *J. Hydrol.* **2019**, *570*, 106–117. [CrossRef]
65. Bazzi, H.; Baghdadi, N.; Fayad, I.; Zribi, M.; Belhouchette, H.; Demarez, V. Near Real-Time Irrigation Detection at Plot Scale Using Sentinel-1 Data. *Remote Sens.* **2020**, *12*, 1456. [CrossRef]
66. Bazzi, H.; Baghdadi, N.; Fayad, I.; Charron, F.; Zribi, M.; Belhouchette, H. Irrigation Events Detection over Intensively Irrigated Grassland Plots Using Sentinel-1 Data. *Remote Sens.* **2020**, *12*, 4058. [CrossRef]
67. El Hajj, M.; Baghdadi, N.; Bazzi, H.; Zribi, M. Penetration Analysis of SAR Signals in the C and L Bands for Wheat, Maize, and Grasslands. *Remote Sens.* **2018**, *11*, 31. [CrossRef]
68. Biemans, H.; Siderius, C.; Mishra, A.; Ahmad, B. Crop-Specific Seasonal Estimates of Irrigation-Water Demand in South Asia. *Hydrol. Earth Syst. Sci.* **2016**, *20*, 1971–1982. [CrossRef]
69. Lopez, O.; Johansen, K.; Aragon, B.; Li, T.; Houborg, R.; Malbeteau, Y.; AlMashharawi, S.; Altaf, M.U.; Fallatah, E.M.; Dasari, H.P.; et al. Mapping Groundwater Abstractions from Irrigated Agriculture: Big Data, Inverse Modeling and a Satellite-Model Fusion Approach. *Hydrol. Earth Syst. Sci.* **2020**, *24*, 5251–5277. [CrossRef]
70. Le Page, M.; Jarlan, L.; El Hajj, M.M.; Zribi, M.; Baghdadi, N.; Boone, A. Potential for the Detection of Irrigation Events on Maize Plots Using Sentinel-1 Soil Moisture Products. *Remote Sens.* **2020**, *12*, 1621. [CrossRef]
71. Dari, J.; Brocca, L.; Quintana-Seguí, P.; Escorihuela, M.J.; Stefan, V.; Morbidelli, R. Exploiting High-Resolution Remote Sensing Soil Moisture to Estimate Irrigation Water Amounts over a Mediterranean Region. *Remote Sens.* **2020**, *12*, 2593. [CrossRef]
72. Calder, T.C. Efficiency of Sprinkler Irrigation Systems. *J. Dep. Agric. West. Aust.* **1976**, *17*, 4.
73. Mu, Q.; Zhao, M.; Running, S.W. Improvements to a MODIS Global Terrestrial Evapotranspiration Algorithm. *Remote Sens. Environ.* **2011**, *115*, 1781–1800. [CrossRef]
74. NASA MODIS Land Evapotranspiration. Available online: https://modis-land.gsfc.nasa.gov/ET.html (accessed on 15 April 2021).
75. Muñoz-Sabater, J.; Dutra, E.; Agustí-Panareda, A.; Albergel, C.; Arduini, G.; Balsamo, G.; Boussetta, S.; Choulga, M.; Harrigan, S.; Hersbach, H.; et al. ERA5-Land: A State-of-the-Art Global Reanalysis Dataset for Land Applications. *Earth Syst. Sci. Data Discuss.* **2021**. [CrossRef]
76. Immitzer, M.; Vuolo, F.; Atzberger, C. First Experience with Sentinel-2 Data for Crop and Tree Species Classifications in Central Europe. *Remote Sens.* **2016**, *8*, 166. [CrossRef]
77. Ji, S.; Zhang, C.; Xu, A.; Shi, Y.; Duan, Y. 3D Convolutional Neural Networks for Crop Classification with Multi-Temporal Remote Sensing Images. *Remote Sens.* **2018**, *10*, 75. [CrossRef]
78. Kussul, N.; Lavreniuk, M.; Skakun, S.; Shelestov, A. Deep Learning Classification of Land Cover and Crop Types Using Remote Sensing Data. *IEEE Geosci. Remote Sens. Lett.* **2017**, *14*, 778–782. [CrossRef]
79. Mathur, A.; Foody, G.M. Crop Classification by Support Vector Machine with Intelligently Selected Training Data for an Operational Application. *Int. J. Remote Sens.* **2008**, *29*, 2227–2240. [CrossRef]
80. Van Tricht, K.; Gobin, A.; Gilliams, S.; Piccard, I. Synergistic Use of Radar Sentinel-1 and Optical Sentinel-2 Imagery for Crop Mapping: A Case Study for Belgium. *Remote Sens.* **2018**, *10*, 1642. [CrossRef]
81. Meroni, M.; d'Andrimont, R.; Vrieling, A.; Fasbender, D.; Lemoine, G.; Rembold, F.; Seguini, L.; Verhegghen, A. Comparing Land Surface Phenology of Major European Crops as Derived from SAR and Multispectral Data of Sentinel-1 and -2. *Remote Sens. Environ.* **2021**, *253*, 112232. [CrossRef] [PubMed]

82. d'Andrimont, R.; Taymans, M.; Lemoine, G.; Ceglar, A.; Yordanov, M.; van der Velde, M. Detecting Flowering Phenology in Oil Seed Rape Parcels with Sentinel-1 and -2 Time Series. *Remote Sens. Environ.* **2020**, *239*, 111660. [CrossRef] [PubMed]
83. Song, Y.; Wang, J. Mapping Winter Wheat Planting Area and Monitoring Its Phenology Using Sentinel-1 Backscatter Time Series. *Remote Sens.* **2019**, *11*, 449. [CrossRef]
84. Veloso, A.; Mermoz, S.; Bouvet, A.; Le Toan, T.; Planells, M.; Dejoux, J.-F.; Ceschia, E. Understanding the Temporal Behavior of Crops Using Sentinel-1 and Sentinel-2-like Data for Agricultural Applications. *Remote Sens. Environ.* **2017**, *199*, 415–426. [CrossRef]
85. Vreugdenhil, M.; Wagner, W.; Bauer-Marschallinger, B.; Pfeil, I.; Teubner, I.; Rüdiger, C.; Strauss, P. Sensitivity of Sentinel-1 Backscatter to Vegetation Dynamics: An Austrian Case Study. *Remote Sens.* **2018**, *10*, 1396. [CrossRef]
86. Bazzi, H.; Baghdadi, N.; Ienco, D.; El Hajj, M.; Zribi, M.; Belhouchette, H.; Escorihuela, M.J.; Demarez, V. Mapping Irrigated Areas Using Sentinel-1 Time Series in Catalonia, Spain. *Remote Sens.* **2019**, *11*, 1836. [CrossRef]
87. Dari, J.; Quintana-Seguí, P.; Escorihuela, M.J.; Stefan, S.; Brocca, L.; Morbidelli, R. Detecting and Mapping Irrigated Areas in a Mediterranean Environment by Using Remote Sensing Soil Moisture and a Land Surface Model. *J. Hydrol.* **2021**, *596*, 126129. [CrossRef]
88. Symbios CEOS EO HANDBOOK—MISSION SUMMARY—Sentinel-1 C. Available online: http://database.eohandbook.com/database/missionsummary.aspx?missionID=577 (accessed on 15 February 2021).
89. Abowarda, A.S.; Bai, L.; Zhang, C.; Long, D.; Li, X.; Huang, Q.; Sun, Z. Generating Surface Soil Moisture at 30 m Spatial Resolution Using Both Data Fusion and Machine Learning toward Better Water Resources Management at the Field Scale. *Remote Sens. Environ.* **2021**, *255*, 112301. [CrossRef]